RSC Advances

PAPER

View Article Online
View Journal | View Issue

Cite this: *RSC Adv.*, 2019, **9**, 33806

The synthesis of $Co_xNi_{1-x}Fe_2O_4$/multi-walled carbon nanotube nanocomposites and their photocatalytic performance†

Min Lu,[a] Yanwei Chang,[a] Xiao-Hui Guan [a] and Guang-Sheng Wang *[b]

Received 12th August 2019
Accepted 2nd October 2019

DOI: 10.1039/c9ra06261k

rsc.li/rsc-advances

A series of $Co_xNi_{1-x}Fe_2O_4$/multi-walled carbon nanotube ($Co_xNi_{1-x}Fe_2O_4$/MWCNTs) nanocomposites as photocatalysts were successfully synthesized, where $Co_xNi_{1-x}Fe_2O_4$ was synthesized *via* a one-step hydrothermal approach. Simultaneously, methylene blue (MB) was used as the research object to investigate the catalytic effect of the catalyst in the presence of hydrogen peroxide (H_2O_2). The results showed that all the photocatalysts exhibited enhanced catalytic activity compared to pure ferrite. In addition, compared with the other photocatalysts, the reaction time was greatly shortened a significantly higher removal rate was achieved using 3-CNF/MWCNTs. There was no significant decrease in photodegradation efficiency after three catalytic cycles, suggesting that $Co_xNi_{1-x}Fe_2O_4$/MWCNTs are recyclable photocatalysts for wastewater treatment. Our results indicate that the $Co_xNi_{1-x}Fe_2O_4$/MWCNT composite can be effectively applied for the removal of organic pollutants as a novel photocatalyst.

1 Introduction

As a new technology in the field of water treatment, photocatalytic technology has attracted considerable attention from researchers worldwide because of its advantages of low energy consumption, environmental friendliness, high efficiency, reusable catalyst and absence of by-products.[1,2] Since Fujishima *et al.*[3] reported that titanium dioxide (TiO_2) can make water undergo continuous oxidation–reduction reaction under irradiation, researchers have been committed to developing novel photocatalysts. However, the industrialization of TiO_2 is limited by its poor dispersion, difficult separation and recovery after photocatalysis, and easy reunion and inactivation.[4–6] Although some other semiconductor materials (such as $SrTiO_3$ and K_4NbO_7)[7–10] have similar photocatalytic properties and stability, they have not become mainstream photocatalysts because of their strong selectivity and large absorption band gap, which are not conducive to the direct absorption and utilization of visible light. Ferrite is a new composite oxide composed of iron and one or more other metals, which can be a ferromagnetic metal oxide.[11–14] According to its lattice type, ferrite can be divided into spinel ferrite, lead ferrite and garnet ferrite. Among them, spinel ferrite, as a new type of semiconductor compound, has the characteristics of narrow band gap, response to visible light, stable photoelectrochemical performance, high reusability, and good photosensitivity and stability.[15–18] It can produce photogenerated electron–hole pairs when irradiated by light, which can lead to redox reactions to achieve the goal of photocatalysis.[19–24] Moreover, spinel ferrites can also catalyze the decomposition of hydrogen peroxide to produce hydroxyl radicals and oxidize organic pollutants such as synthetic dyes in water.[25,26] Although enormous progress has been already achieved in the integration of ferrites to improve the photocatalytic performance of materials, more attention should be focused on further enhancing the adsorption capacity and promoting the separation rate of photogenerated electron–hole pairs to substantially expand the application field of photocatalysts.[27–30]

Carbon nanotubes (CNTs), as one-dimensional nanomaterials, are hollow tubular structures consisting of carbon element. According to the number of layers of graphene sheets, CNTs include single-walled carbon nanotubes (SWCNTs) and multi-walled carbon nanotubes (MWCNTs).[31,32] sp^2 hybridized carbon atoms are mainly present in CNTs. Moreover, because of a certain degree of curvature, the hexagonal grid structure forms a spatial topological structure, in which a certain sp^3 hybrid bond can be formed. A large number of chemical bonds on the outer surface of CNTs are the basis of bonding between CNTs and some macromolecular complexes with non-covalent bond conjugation properties.[33–36] Therefore, CNTs have many unique mechanical, electrical and chemical properties due to their light weight and perfect hexagonal connection in the fields of composite materials, hydrogen storage, electronic devices, batteries, supercapacitors, field-emission displays, quantum wire template electron guns, sensors and microscopic probes.[37–41] In recent years, in order to

[a]*School of Chemical Engineering, Northeast Electric Power University, Jilin 132000, P. R. China*

[b]*Key Laboratory of Bio-Inspired Smart Interfacial Science and Technology of Ministry of Education, School of Chemistry, Beihang University, Beijing 100191, PR China. E-mail: wanggsh@buaa.edu.cn*

† Electronic supplementary information (ESI) available. See DOI: 10.1039/c9ra06261k

further expand the response range of catalysts in the solar spectrum, carbon-based semiconductor catalysts with excellent performance have been synthesized by combining carbon materials and semiconductors, resulting in fast electron conductivity, large specific surface area, high optical transparency, and high thermal conductivity. Carbon materials play a vital role in the utilization of solar energy.[42–46] Because carbon materials as catalysts produce free radicals under ultraviolet radiation, they can improve the catalytic performance and promote the degradation of organic pollutants *via* the interaction of carbon and light.[47,48] Therefore, assembling $Co_xNi_{1-x}Fe_2O_4$ particles on MWCNTs to prepare a novel carbon-based photocatalyst, $Co_xNi_{1-x}Fe_2O_4$/MWCNTs, is greatly significant to improve the photocatalytic performance and application in environmental remediation.[49,50]

Herein, we report the fabrication of $Co_xNi_{1-x}Fe_2O_4$/MWCNT composites *via* the hydrothermal method. Subsequently, the photodegradation efficiency by the synthesized photocatalyst in the presence of hydrogen peroxide (H_2O_2) was investigated with methylene blue (MB) as the removal object. Furthermore, all the prepared composites were characterized using modern analytical methods. According to the final results, the photocatalytic performance of all the carbon-based photocatalysts is better than that of pure ferrite.

2 Experimental

2.1 Materials

All reagents were of analytical grade and used as received without further purification. MWCNTs were purchased from Yongda Chemical Reagent Development Center (Beijing). The purity of the MWCNTs was more than 95 wt% and their outer and inner diameters were 8–15 and 3–5 nm, respectively with a length of approximately 50 μm. Before the decoration, the MWCNTs were dispersed in a mixture of concentrated sulfuric acid and nitric acid (3 : 1 by volume), loaded in a 100 mL high-pressure reactor and heated at different temperatures and times in to optimize the reaction conditions. Subsequently, the prepared solid products were centrifuged, washed several times and oven-dried at 60 °C.

2.2 Synthesis of $Co_xNi_{1-x}Fe_2O_4$/MWCNT composites

Firstly, a certain amount of FCl_2, $CoCl_2$, $NiCl_2$ and $FeCl_3 \cdot 6H_2O$ were weighed. Subsequently, MWCNTs with a mass fraction of 20% and 60 mL glycol and 4 mmol $CO(NH_2)_2$ were added to the chamber of the PTFE reactor under ultrasonication for 20 min. Then, the mixture was hydrothermally treated at 180 °C for 5 h in an oven. After the reaction was complete, the autoclave was cooled to room temperature and the supernatant was discarded. The supernatant was washed at least three times with desalted water and ethanol. The autoclave was dried for 12 h in a vacuum drying chamber at 60 °C. After drying, the sample was ground in a mortar and placed in a sample tube (Fig. S1†).

2.3 Characterization

The morphology and size of the samples were determined by scanning electron microscopy (SEM, Quanta200, Holland). Transmission electron microscopy (TEM) and high-resolution TEM (HRTEM) were carried out using a JEOL JEM-2100F microscope. The crystallization of the products was examined by X-ray diffraction (XRD, XRD-7000, Japan) with Cu-KR radiation. Raman spectroscopy was performed with 632.5 nm wavelength incident laser light. The specific surface area of the samples was tested on a volumetric gas sorption instrument (BET, ASAP2020, America). The optical properties of the photocatalysts were investigated using a UV-2550 spectrophotometer.

2.4 Photocatalytic experiments

The photocatalytic degradation of MB by the synthesized photocatalyst was evaluated in a home-made reactor using a 300 W xenon lamp as the light source. Firstly, 0.05 g photocatalyst was injected into 100 mL MB solution was a concentration of 50 mg L^{-1} under stirring. Subsequently, the solution was stirred in the dark for 55 minutes after ultrasonication for 5 min, which reached adsorption and desorption equilibrium. Then, 1 mL H_2O_2 was added to the above solution, and the reaction took place in a reactor placed 66 cm away from the Xe lamp. Photoirradiation was carried out using a Xe lamp of 300 W through UV cut-off filters (JB450) to completely remove any radiation below 420 nm and to ensure illumination by visible light only. Primarily, the stability of the visible light source was ensured using the Xe lamp. Finally, at regular intervals, 1 mL of solution was withdrawn and diluted to 6 mL with distilled water. The residual sample was removed by centrifugation. The concentration of MB was analyzed using a UV-vis adsorption spectrometer at 663 nm. The pH, dose of H_2O_2, photocatalyst dosage, and initial dye concentration as the parameters in the reaction process were varied.

3. Results and discussion

3.1 Morphology and structure analysis of samples

The X-ray diffraction (XRD) patterns of the samples are shown in Fig. 1. The XRD pattern of 1-CNF shows that all the diffraction peaks are characteristic of Fe_3O_4 with the standard Joint Committee on Powder Diffraction Standards (JCPDS)

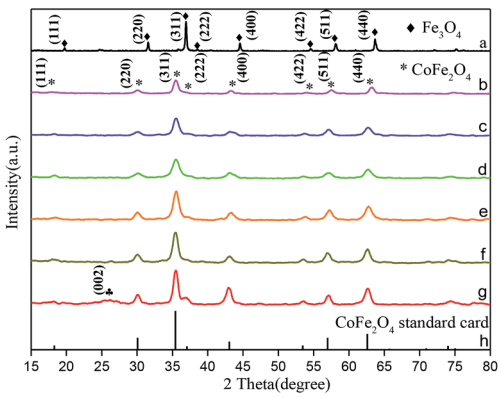

Fig. 1 XRD of patterns of CNF and 3-CNF/MWCNTs. (a) 1-CNF, (b) 2-CNF; (c) 3-CNF, (d) 4-CNF, (e) 5-CNF, (f) 6-CNF, (g) 3-CNF/MWCNTs, and (h) $CoFe_2O_4$ standard card.

card no. 75-0449 (Fig. 1a). The concentration of Co^{2+} and Ni^{2+} was adjusted to synthesize $Co_xNi_{1-x}Fe_2O_4$, as shown in eqn (1)–(6). From the XRD patterns of samples from 2-CNF to 6-CNF (Fig. 1b–f), all the diffraction peaks are in good agreement with the standard Joint Committee on Power Diffraction Standards (JCPDS) card no. 22-1086 (Fig. 1h), corresponding to the planes of (111), (200), (222), (311), (400), (422) (511), and (440), respectively. The radius of the Co^{2+} ions ($r = 0.089$ nm at O_h) is similar to that of Ni^{2+} ions ($r = 0.083$ nm at O_h). Therefore, the Co^{2+} ions at O_h could be effectively substituted for Ni^{2+} ions without a change in the lattice constant, indicating that no peak positions were shifted. Nevertheless, in the XRD patterns of 3-CNF/MWCNTs (Fig. 1g), it can be seen that the additional diffraction peak at $2\theta = 26.4^\circ$ is estimated to be the (002) plane of the MWCNTs. The average crystallite size was obtained from the Scherrer formula applied to the major peak ($\theta = 311$), which was estimated to be around 16.6 nm for the samples under investigation.

$$CO(NH_2)_2(aq) + H_2O(aq) \rightarrow CO_2(aq) + 2NH_3(aq) \quad (1)$$

$$NH_3(aq) + H_2O(aq) \rightarrow NH_3\cdot H_2O(aq) \quad (2)$$

$$NH_3\cdot H_2O(aq) \rightleftharpoons NH_4^+(aq) + OH^-(aq) \quad (3)$$

$$Co^{2+}(aq) + 6NH_3\cdot H_2O(aq) \rightleftharpoons [Co(NH_3)_6]^{2+} + 6H_2O \quad (4)$$

$$Ni^{2+}(aq) + 6NH_3\cdot H_2O(aq) \rightleftharpoons [Ni(NH_3)_6]^{2+} + 6H_2O \quad (5)$$

$$2Fe^{3+}(aq) + xCo^{2+}(aq) + (1-x)Ni^{2+}(aq) + 4H_2O \rightarrow Co_xNi_{1-x}Fe_2O_4(s) + 8H^+(aq) \quad (6)$$

The selected area electron diffraction pattern (SAED) of 3-CNF/MWCNTs is shown in Fig. 2, which suggests the polycrystalline structure of the sample. The series of circular arcs correspond to the diffraction peaks of 3-CNF/MWCNTs in Fig. 1g, indicating each crystal surface of 3-CNF/MWCNTs. The (111), (220), (311), (222), (400), (511) and (440) reflection planes of 3-CNF/MWCNTs correspond to the *d*-spacings of 0.490 nm, 0.295 nm, 0.253 nm, 0.242 nm, 0.210 nm, 0.160 nm and 0.147 nm, respectively. The (002) reflection plane of MWCNTs corresponds to the *d*-spacing of 0.337 nm.

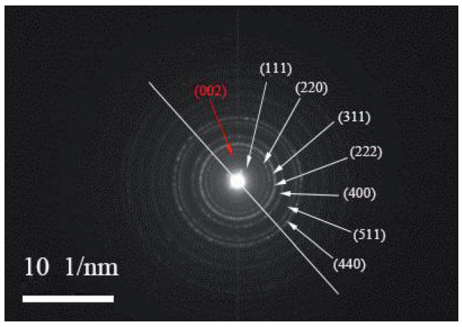

Fig. 2 Selected area electron diffraction pattern of 3-CNF/MWCNTs.

The SEM image (Fig. S2†) indicates that the samples were spherical-like particles with the introduction of the nickel source in the preparation of Fe_3O_4 and $Co_xNi_{1-x}Fe_2O_4$ *via* the solvothermal method. With an increase in the Ni content, the particle size increased slightly. The particle size of $NiFe_2O_4$ was about 19 nm until Ni completely replaced Co. However, the ferrite particle size was small, and agglomeration was serious, which limit its application. Therefore, multi-walled carbon nanotubes (MWCNTs) were considered as carriers for the preparation of composite materials to improve the dispersion of the ferrites and expose them to more active sites. The SEM images (Fig. S3†) show the distribution of the different $Co_xNi_{1-x}Fe_2O_4$ on MWCNTs. When Ni was not added, a large amount of agglomerated and flaky cobalt ferrite accumulated on the MWCNTs (Fig. S3a†). With the gradual addition of Ni, the lamellar structure of cobalt–nickel ferrite disappeared and uniform nanospheres were coated on the surface of the MWCNTs. Also, cobalt–nickel ferrite was uniformly dispersed and closely bonded on the multi-walled carbon nanotubes to minimize the agglomeration of ferrite (Fig. S3b–d†). When Ni completely replaced Co, the particle size of nickel ferrite increased gradually and the coating effect on the MWCNTs decreased (Fig. S3e†). The composition of the as-prepared sample 3-CNF/MWCNTs was verified by EDS spectroscopy (Fig. S4† and Table 1), which shows the nanocomposites contained only Co, Ni, Fe, C and O, and the whole nanostructure was uniform.

The sizes and morphologies of the as-prepared nanocomposites were further determined using TEM and HRTEM. Obviously, the TEM image (Fig. 3a) also confirms that most of the MWCNTs were completely coated with 3-CNF. Furthermore, the distribution of these nanoparticles on the MWCNT surface was quite uniform and no detectable local aggregation was observed. The narrow particle size distribution and size of the MWCNTs are 16 nm and 10–17 nm, respectively. It is known from TEM that the size of the ferrite is 16 nm, which is consistent with the results obtained by the Scherrer formula. Meanwhile, the HRTEM image (Fig. 3b), which was taken from the selected area marked in Fig. 3a, reveals that 3-CNF nanocrystals have a polycrystalline structure. Fig. 3c shows that the singular spacing of the nanocrystals of 3-CNF is 0.262 nm, which is nearly consistent with the (311) reflection plane spacing of 3-CNF/MWCNTs.

To further demonstrate that $Co_xNi_{1-x}Fe_2O_4$ was effectively coated on the MWCNTs, the oxidized MWCNT and 3-CNF/

Table 1 The mole ratio of the as-prepared samples

Serial number	The mole ratio of Co : Ni : Fe	Sample
1	0.00 : 0.00 : 3.0	1-CNF
2	1.00 : 0.00 : 2.00	2-CNF
3	0.75 : 0.25 : 2.00	3-CNF
4	0.50 : 0.50 : 2.00	4-CNF
5	0.25 : 0.75 : 2.00	5-CNF
6	0.00 : 1.00 : 2.00	6-CNF

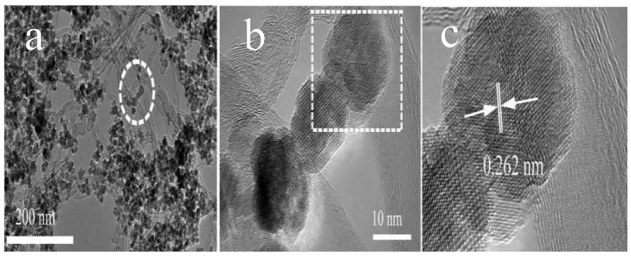

Fig. 3 (a) TEM image of the 3-CNF/MWCNTs, (b) HRTEM image of the selected area marked by a circle in (a and c) enlarged HRTEM image of the selected area marked by a square in (b).

MWCNT nanocomposites were investigated using Raman spectroscopy in the frequency range of 0–2000 cm^{-1} at room temperature (Fig. 4a). Both them exhibited two characteristic peaks in the frequency range of 1000–2000 cm^{-1}. One of the intense features is the G peak at 1581 cm^{-1}, which is due to the doubly degenerate zone center E_{2g} mode and reflects the sp^2 hybridization intensity of the carbon atoms in the MWCNTs. Simultaneously, the other characteristic peak is the D peak at 1348 cm^{-1}, which is attributed to the presence of amorphous or disordered carbon in the MWCNTs. It is obvious that both characteristic peaks showed the degree of defects on the surface of the MWCNTs. Further, calculating the areas of the D and G peaks for both samples, the greater the I_D/I_G ratio, the more crystal defects. The ratios were calculated to be 1.36 and 1.34 before and after coating, respectively, which fully illustrate that the defects on the surface of the MWCNTs were still retained to provide more sites for adsorption. The investigation of the various peaks observed in the Raman spectra in the low wavenumber range of 100–800 cm^{-1} is shown in Fig. 4b. To ascertain the natural frequency, line width and lattice strain effect, the spectra were fitted using least squares method fitting with Lorentzian line shape. With the doping of Ni in $CoFe_2O_4$, $Co_xNi_{1-x}Fe_2O_4$ still crystallized in the AB_2O_4-type spinel structure belonging to the space group O_h,[7] which is composed of five Raman active phonon modes, namely $A_{1g} + E_g + 3T_{2g}$ consisting of O ions as anions and both A-site and B-site ions as cations, respectively. The Raman active phonon modes of T_{2g}^{1} (1) (ω = 193 cm^{-1}), T_{2g}^{2} (ω = 564 cm^{-1}) and T_{2g}^{3} (ω = 478 cm^{-1}) were included in the category of $3T_{2g}$. The spectra consist of broad bands at 144 cm^{-1}, 193 cm^{-1}, 327 cm^{-1}, 478 cm^{-1}, 564 cm^{-1}, 632 cm^{-1} and 690 cm^{-1}. According to the literature, there were no shoulder-like features assigned to Fe_3O_4 in the low frequency range; however, the strong band at 690 cm^{-1} shows a shoulder-like feature at 632 cm^{-1}, which reflects the stretching vibration of the Fe^{3+} and O^{2-} ions in the tetrahedral site of the A_{1g} modes. Meanwhile, the lower frequency mode is assigned to the T_{2g} mode with a shoulder-like feature, indicating the absence of Fe_3O_4.

XPS is one of the surface analytical techniques used to provide information on the functional groups and surface detects of the 3-CNF/MWCNT nanocomposite. Also, the detail binding energies were obtained by Gaussian fitting. In Fig. 5a, the deconvolution of the Co2p, Ni2p, Fe2p, C1s and O1s peaks of the nanocomposites showed the main peaks. All of the Co2p (778.3 eV), Ni2p (852.6 eV) and Fe2p (706.9 eV) peaks were derived from $Co_xNi_{1-x}Fe_2O_4$. The C1s peak demonstrates the presence of MWCNTs. The O1s peak is attributed to the carboxylic, hydroxyl (533.1 eV) and ester (531.9 eV) functional groups and $Co_xNi_{1-x}Fe_2O_4$ (529.8 eV) on the surface of the MWCNTs. The Co2p spectra (as shown in Fig. 5b) consist of two spin–orbit doublets characteristic of $Co2p_{3/2}$ (Co^{2+} in Oct-site, 779.7 eV; Co^{2+}, Tet-site, 781.2 eV; and Co^{3+} in Oct-site, 782.9 eV) and $Co2p_{1/2}$ (Co^{2+} in Oct-site, 759.7 eV; Co^{2+}, Tet-site, 796.9 eV; and Co^{3+} in Oct-site, 798.8 eV), and two shakeup satellites at 786.9 eV and 803 eV. The Ni2p spectra in Fig. 5c also display two spin–orbit doublets characteristic of $Ni2p_{3/2}$ (Ni^{2+} in Oct-site, 854.8 eV; Ni^{3+},

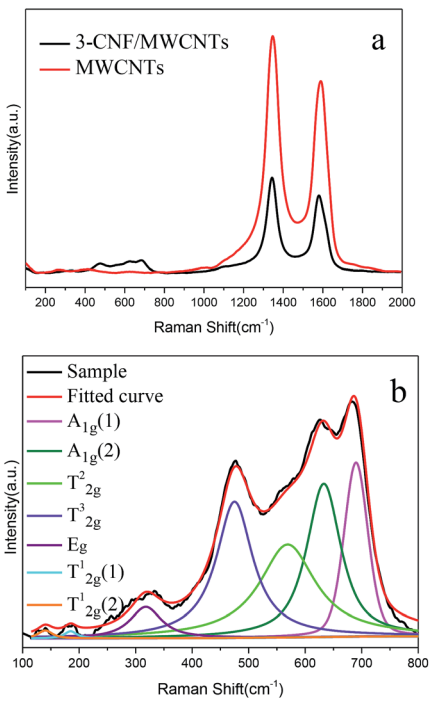

Fig. 4 Raman spectra (a) MWCNTs and 3-CNF/MWCNTs and (b) 3-CNF/MWCNTs in the low wavenumber range of 100–800 cm^{-1}.

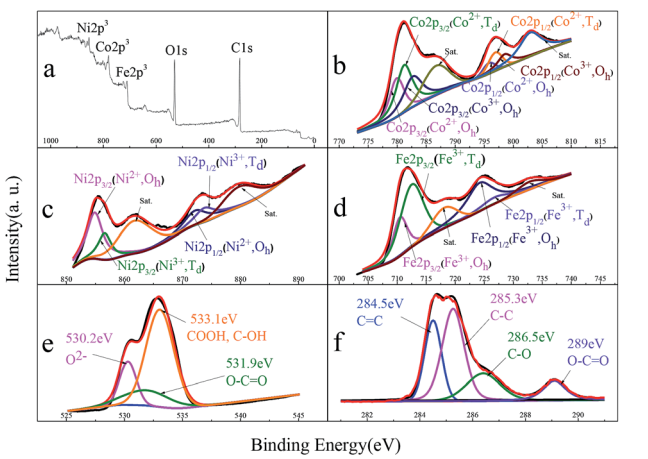

Fig. 5 XPS of 3-CNF/MWCNTs (a) 3-CNF/MWCNT nanocomposite (b) Co2p, (c) Ni2p, (d) Fe_2p, (e) O1s and (f) C1s.

Tet-site, 856.5 eV) and Ni2p$_{1/2}$ (Ni^{2+} in Oct-site, 872.2 eV; Ni^{3+}, Tet-site, 784.0 eV) with two shakeup satellites at 861.8 eV and 880.0 eV. The observed satellites and asymmetry of the Co2p$_{1/2}$ and Ni2p$_{1/2}$ peaks demonstrate the existence of Co^{2+}/Co^{3+} and Ni^{2+}/Ni^{3+} in the nanocomposites. The Fe2p spectra in Fig. 5d had two spin–orbit doublets of Fe2p$_{3/2}$ (Fe^{3+} in Oct-site, 710.6 eV and Fe^{3+}, Tet-site, 712.8 eV) and Fe2p$_{1/2}$ (Fe^{3+} in Oct-site, 724.4 eV and Fe^{3+}, Tet-site, 726.9 eV), and two shakeup satellites at 718.1 eV and 732.9 eV, which are essentially the same in the Co2p and Ni2p spectra. Fig. 5e shows a peak at 530.2 eV, which is assigned to lattice O^{2-} in the M–O bonds (M = Co, Ni, and Fe) and the second peak at 531.9 eV indicates the presence of O–C=O. The functional groups such as carboxyl and hydroxyl are responsible for the peak at 533.1 eV. There are two main peaks in the C1s spectra (Fig. 5f). The main peak at 284.5 eV in the C1s spectra was attributed to C=C in the form of sp^2 hybridized, which characterizes the graphitic structure of the MWCNTs. The other peak at 285.3 eV is attributed to C–C in the form of sp^3 hybridized, which indicates the defect structure of the MWCNTs. The peaks at 286.5 eV and 289 eV illustrate the presence of C–O and O–C=O, respectively, which are further evidence of the acid oxidation in MWCNTs. Ultimately, the surface composition calculated by XPS was ($Co_{0.46}^{2+}Ni_{0.19}^{3+}Fe_{1.4}^{3+}$) [$Co_{0.3}^{2+}Ni_{0.43}^{2+}Co_{0.36}^{3+}Fe_{0.6}^{3+}$]$O_4$/MWCNTs.

The N_2 adsorption–desorption isotherms of $CoNiFe_2O_4$ and $CoNiFe_2O_4$/MWCNTs are presented in Fig. 6. The composite displays the typical type-4 isotherm with the hysteresis loop near the P/P_0 value of 1.0, which demonstrates its mesoporous structure. The BET surface areas of the 3-CNF nanospheres and 3-CNF/MWCNTs were 29.64 $m^2\ g^{-1}$ and 157.27 $m^2\ g^{-1}$, respectively, demonstrating that the nanocomposite was required to improve the adsorption properties.

The hysteresis loops of the as-synthesized samples were also measured at 300 K (Fig. 7). The hysteresis loops almost passed through the origin, *i.e.* coercivity and residual magnetization were almost zero, which indicates that they are super-paramagnetic materials. The saturation magnetization of 3-CNF and 3-CNF/20%MWCNTs was 95.30 emu g^{-1} and 44.03 emu g^{-1}, respectively. When the sample was added to the wastewater solution as a photocatalyst, the nanocomposite was easily separated from the dye wastewater by magnetic separation techniques, which greatly reduced the difficulty of separation.

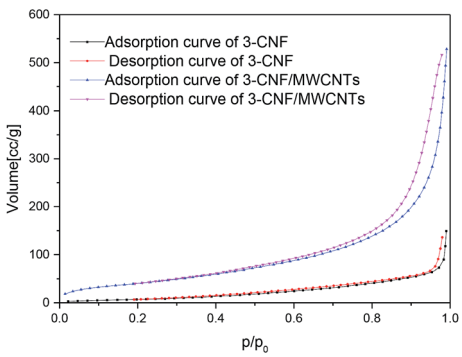

Fig. 6 N_2 adsorption–desorption isotherms of 3-CNF and 3-CNF/MWCNTs.

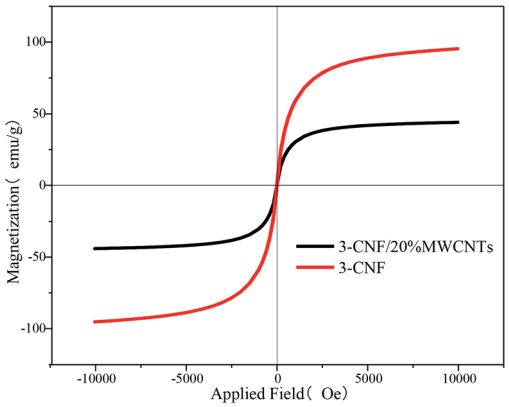

Fig. 7 Magnetic hysteresis loops for 3-CNFand 3-CNF/MWCNTs.

3.2 Photocatalytic performance of the samples

The effect of catalyst dosage on the degradation of MB was observed by adding 0.2, 0.5 and 0.7 g of 3-CNF/MWCNT catalyst to 100 mL of MB solution in a reactor. Fig. S5† shows that the degradation rate increased with an increase in the catalyst dosage, which is a characteristic of heterogeneous photocatalysis. The reason for this is the improvement in available active sites and hydroxyl radical (˙OH). Here, 0.5 g of catalyst was added to 100 mL of dye solution with different initial concentrations (20, 50 and 80 mg L^{-1}) (Fig. S6†). As the initial concentration of the dye increased, the number of dye molecules also increased with a fixed number of active photocatalyst sites. Thus, the rate of degradation decreased. It is well known that the dose of H_2O_2 is a key parameter in Fenton or Fenton-like reactions. Generally, a low concentration of H_2O_2 can be easily depleted, resulting in difficulty to produce ˙OH continuously, and then the degradation of pollutants is suppressed. When the dosage was 1.5 mM, the degradation time was the shortest. The degradation of MB decreased with an increase in H_2O_2 concentration up to 4.0 mM. A high dose of H_2O_2 over 4.0 mM in the experiments may be a scavenger of ˙OH, thus hindering the degradation of MB (Fig. S7†). The degradation of MB by the 3CNF/MWCNT nanocomposite was also investigated in the pH range of 3.0 to 12.0 (Fig. S8†). The pH of the solution of the dye has a great influence on the degradation.[51] The degradation of the dyes was lower in acidic solution (pH 3.0 and pH 5.0) and neutral solution (pH 7.0) than in basic solution (pH 12.0). The dye molecules are adsorbed more by the negatively charged 3CNF/MWCNT surface at pH 12, and hence the degradation efficiency is higher at this pH. The hydroxyl radical (˙OH) density is presumably greater on the catalyst surface, where it is formed, which promotes the degradation of MB in solution. On the other hand, the catalyst surface also exerts a negatively charged surface at the solution pH > pHzpc.[52] Hence, the coulombic attraction between the dye cations and the negatively charged catalyst surface increases the adsorption of the dye onto the catalyst surface.

Under light irradiation, the photocatalytic activity of the $Co_xNi_{1-x}Fe_2O_4$/multi-walled carbon nanotube nanocomposites was assessed with H_2O_2 by photocatalytic degradation of MB

solution. As shown in Fig. 8a, in the initial 60 min when the reaction was performed in the dark with the addition of H_2O_2, the adsorption process of the nanocomposite occurred primarily, during which the MB solution reached the adsorption–desorption equilibrium. Obviously, the nanocomposites with a higher content of Ni in ferrite exhibited a higher adsorption efficiency. In the first 60 min, the adsorption rates of the nanocomposites were 37.21%, 48.22%, 49.31%, 52.0% and 58.96%, respectively. However, the adsorption rate for pure ferrite (3-CNF) was only 8.94%, indicating that the addition of MWCNTs substantially improved the adsorption capacity of the nanocomposites and further increased the removal efficiency of MB molecules. For example, the removal rates of MB were 96.51%, 99.93%, 98.19%, 97.07% and 97.29% from 2-CNF/MWCNTs to 6-CNF/MWCNTs, which were higher than that of 87.44% for pure ferrite. Also, for pure ferrite, it was difficult for the degradation rate of MB molecules reached 99% in 100 min. In addition, all the multi-walled carbon nanotube nanocomposites showed superior photocatalytic performances than pure ferrite. Furthermore, among the prepared photocatalysts, 3-CNF/MWCNTs could greatly shorten the reaction time and exhibited a significantly higher removal rate. Thus, for practical application, it is perfectly reasonable to speculate that 3-CNF/MWCNTs is the most appropriate photocatalyst. The results of the blank experiments are shown in Fig. 8b. Based on the adsorption experiment of 3-CNF/MWCNTs (Fig. 8b) without illumination, 3-CNF/MWCNTs reached adsorption–desorption equilibrium within 40 min. However, it can be seen from the results of the photocatalytic reaction that 3-CNF/MWCNTs in the presence of light irradiation (Fig. 8b) displayed a higher MB removal rate than other conditions, illustrating that the degradation of MB molecules is primarily attributed to the photocatalytic activity of 3-CNF/MWCNTs. As shown in Fig. 8b, the removal rate of MB was about 65% in the presence of 3-CNF/MWCNTs and H_2O_2 without light irradiation, mostly owing to the adsorption capacity of MWCNTs and the oxidative capacity of H_2O_2. The stability test of 3-CNF/MWCNTs was carried out for the photodegradation of MB under illumination, as shown in Fig. 8c. After reuse, each time, the adsorption efficiency of 3-CNF/MWCNTs was only reduced slightly, indicating that the MB molecules that were adsorbed on the surface of the photocatalyst were finally decomposed. Moreover, after reuse for five cycles, there was no obvious decrease in the photodegradation efficiency, indicating that 3-CNF/MWCNTs is a promising photocatalyst for recyclable utilization. Simultaneously, the stability of the sample is very important for its practical application; therefore, the XRD pattern of 3-CNF/MWCNTs was measured after the reaction (Fig. S9†). Compared with the XRD pattern before the reaction, it was found that there was no obvious change in the photocatalyst.

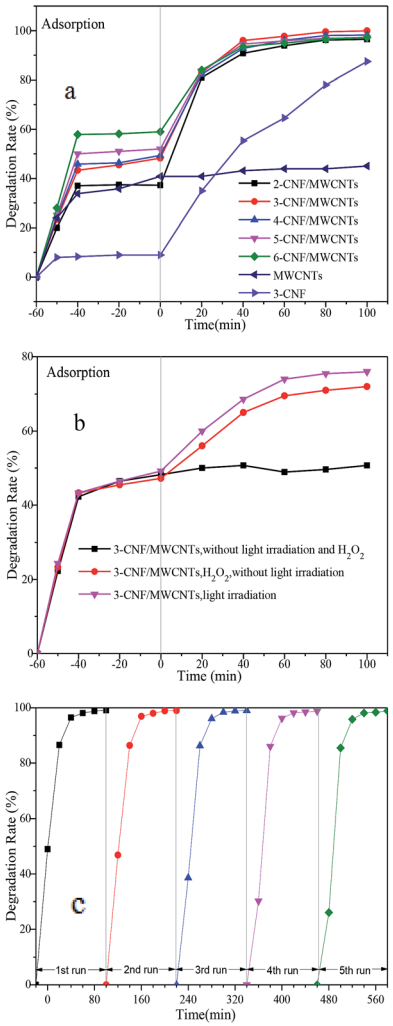

Fig. 8 (a) Degradation rate of MB in the presence of the different samples with H_2O_2, (b) removal rate of MB in the presence of 3-CNF/MWCNTs without light irradiation, 3-CNF/MWCNTs + H_2O_2 without light irradiation and 3-CNF/MWCNTs with light irradiation and (c) repetitive use of 3-CNF/MWCNTs.

3.3 Photocatalytic mechanism

For the photocatalytic degradation of organic dyes, the widely accepted theory is that the degradation of organic dyes is achieved through the generation of $^{\bullet}OH$ by light. When CNF/MWCNTs are used as photocatalysts, CNF is the acceptor of photogenerated electrons and MWCNTs the absorber of light source, the work function of which is much higher than that of semiconductor. Therefore, due to the close contact between the CNF microspheres and MWCNTs and the extremely high carrier migration rate of MWCNTs, more electrons can be transferred between them, which greatly reduces the recombination probability of electrons and holes, resulting in more free electrons in solution. These electrons can transform dissolved oxygen into O^{2-}, which reacts with H_2O to form hydroxyl radicals that can mineralize MB. The photocatalytic degradation of MB by CNF/MWCNTs is illustrated in Fig. S10.†

$$Co_xNi_{1-x}Fe_2O_4 + h\nu \rightarrow Co_xNi_{1-x}Fe_2O_4(h^+ + e) \quad (7)$$

$$Co_xNi_{1-x}Fe_2O_4(e) + MWCNTs \rightarrow Co_xNi_{1-x}Fe_2O_4 + MWCNTs(e) \quad (8)$$

$$MWCNTs(e) + O_2 \rightarrow O_2^{\bullet -} + MWCNTs \quad (9)$$

$$O_2^{\bullet -} + H_2O \rightarrow HO_2^{\bullet} + OH^- \quad (10)$$

$$HO_2^{\bullet -} + H_2O \rightarrow H_2O_2 + {}^{\bullet}OH \quad (11)$$

$$H_2O_2 \rightarrow 2{}^{\bullet}OH \quad (12)$$

$$Co_xNi_{1-x}Fe_2O_4(h^+) + OH \rightarrow Co_xNi_{1-x}Fe_2O_4 + {}^{\bullet}OH \quad (13)$$

$$\text{Dye} + {}^{\bullet}OH \text{ (or } O_2^{\bullet -}) \rightarrow \text{intermediate} \rightarrow CO_2 + NO_3^- + SO_4^{2-} + H^+ + H_2O \quad (14)$$

To further study the mechanism of photocatalytic degradation of MB, EDTA-2Na, TBA and BQ as reducing agents were used to deplete the h^+, $^{\bullet}OH$ and $O2^{\bullet -}$ produced in the process of photocatalytic reaction (Fig. S11†).[53] After 100 min of photocatalytic reaction, the degradation rate of MB by the different reducing agents decreased to varying degrees. As a result, the $OH^{\bullet}$ produced in the photocatalytic reaction was the main active radical, which led to the rapid oxidation of the MB dye molecules.

4 Conclusion

In conclusion, a series of $Co_xNi_{1-x}Fe_2O_4$/MWCNT nanocomposites as photocatalysts was successfully synthesized *via* the hydrothermal method. All the carbon-based composites showed more outstanding photocatalytic performances than pure ferrite. In addition, utilizing 3-CNF/MWCNTs to remove MB greatly shortened the reaction time and resulted in a significantly higher removal rate compared with the other prepared photocatalysts. There was no significant decrease in photodegradation efficiency after reuse for three cycles, suggesting that $Co_xNi_{1-x}Fe_2O_4$/MWCNTs is a promising photocatalyst for recyclable utilization. The results demonstrate that the $Co_xNi_{1-x}Fe_2O_4$/MWCNT composites used as novel photocatalysts have enormous potential for the photodegradation of organic pollutants.

Conflicts of interest

There are no conflicts to declare.

Acknowledgements

This project was financially supported by the National Natural Science Foundation of China (No. 51672040 and 51672013), Science and Technology Research Projects of the Education Department of Jilin Province (JJKH20180429KJ), Jilin City Science and Technology Bureau (201750228).

Notes and references

1 G. Odling and N. Robertson, *Catal. Sci. Technol.*, 2019, **9**, 533–545.
2 P. Mishra, S. Patnaik and K. Parida, *Catal. Sci. Technol.*, 2019, **9**, 1–55.
3 A. Fujishima and K. Honda, *Nature*, 1972, **238**, 37–38.
4 M. B. Askari, Z. T. Banizi and S. Soltani, *Optik*, 2018, **157**, 230–239.
5 J. Zhang, F. X. Xiao, G. Xiao and B. Liu, *Nano*, 2014, **6**, 11293–11302.
6 Z. Durmus, A. Durmus and H. Kavas, *J. Mater. Sci.*, 2015, **50**, 1201–1213.
7 D. Moitra, M. Chandel and B. K. Ghosh, *RSC Adv.*, 2016, **6**, 97941–97952.
8 K. T. Lee, X. F. Chuah and Y. C. Cheng, *J. Mater. Chem. A*, 2015, **36**, 18578–18585.
9 M. Rahimi-Nasrabadi, M. Behpour, A. Sobhani-Nasab and M. R. Jeddy, *J. Mater. Sci.: Mater. Electron.*, 2016, **27**, 11691–11697.
10 P. M. A. Caetano, A. S. Albuquerque and L. E. Fernadez-Outon, *J. Alloys Compd.*, 2018, **758**, 247–255.
11 S. Z. Lin and S. H. Wang, *Dong Bei Dian Li Da Xue Xue Bao*, 2016, **36**(3), 69–74.
12 R. Liu, P. Lv and H. Fu, *J. Nanosci. Nanotechnol.*, 2017, **17**, 4755–4762.
13 E. Alarfaj, S. Hcini and A. Mallah, *J. Supercond. Novel Magn.*, 2018, **1**, 1–10.
14 R. S. Melo, P. Banerjee and A. Franco, *J. Mater. Sci.: Mater. Electron.*, 2018, **26**, 1–11.
15 S. U. Bhasker, G. N. Rao and F. C. Chou, *J. Magn. Magn. Mater.*, 2018, **452**, 398–406.
16 M. J. Sun, X. Q. Wang and R. K. Jia, *J Northeast Electr. Pow. Uni.*, 2010, **30**(1), 35–38.
17 H. Y. He, *J. Part. Sci. Technol.*, 2016, **34**, 143–151.
18 Z. Wu, R. Zhang and Z. Yu, *Ferroelectrics*, 2018, **523**, 82–88.
19 T. Tan, W. Xie and G. Zhu, *J. Porous Mater.*, 2015, **22**, 659–663.
20 B. D. Fellows, S. Sandler, J. Livingston, K. Fuller, L. Nwandu and S. Timmins, *IEEE Magn. Lett.*, 2018, **9**, 1–5.
21 H. Y. Liu and Y. S. Li, *Mater. Sci. Eng.*, 2018, **292**, 012–062.
22 R. R. Bhosale, *Ceram. Int.*, 2018, **44**, 8679–8683.
23 W. W. Aji and E. Suharyadi, *Mater. Sci. Forum*, 2017, **901**, 142–148.
24 V. Anjana, S. John and P. Prakash, *Mater. Sci. Eng.*, 2018, **310**, 012–024.
25 Y. Fu, H. Chen and X. Sun, *Appl. Catal., B*, 2012, **111**, 280–287.
26 O. Raina and R. Manimekalai, *Res. Chem. Intermed.*, 2018, **44**, 5941–5951.
27 S. Kalikeri and V. S. Kodialbail, *Environ. Sci. Pollut. Res.*, 2018, **25**, 1–13.
28 A. Silambarasu, A. Manikandan and K. Balakrishnan, *J. Supercond. Novel Magn.*, 2017, **30**, 1–10.
29 D. Zhang, B. Pan and R. L. Cook, *Environ. Pollut.*, 2015, **196**, 292–299.
30 T. Ketolainen, V. Havu and M. Puska, *J. Chem. Phys.*, 2015, **14 2**, 054–705.
31 K. Anitha, S. Namsani and J. K. Singh, *J. Phys. Chem. A*, 2015, **119**, 8349.
32 P. Sahoo, R. G. Shrestha and L. K. Shrestha, *J. Inorg. Organomet. Polym.*, 2016, **26**, 1–8.
33 A. H. Ashour, A. I. El-Batal and M. I. A. A. Maksoud, *Particuology*, 2018, **40**, 141–151.

34 I. A. F. D. Medeiros, V. Madigou and A. L. Lopes-Moriyama, *J. Nanopart. Res.*, 2018, **20**, 3–8.
35 K. V. Sankar, S. Shanmugapriya and S. Surendran, *J. Colloid Interface Sci.*, 2017, **513**, 480–488.
36 H. Hosseini and H. Mahdavi, *Appl. Organomet. Chem.*, 2018, **32**, e4294.
37 A. B. Nawale, N. S. Kanhe and S. A. Rauta, *Ceram. Int.*, 2017, **43**, 6637–6647.
38 X. Zhao, Y. Fu and J. Wang, *Electrochim. Acta*, 2016, **201**, 172–178.
39 Y. M. Zhang, P. L. Xu and Q. Zeng, *Mater. Sci. Eng., C*, 2017, **74**, 62–69.
40 C. Singh, Devika and R. Malik, *RSC Adv.*, 2015, **108**, 89327–89337.
41 J. Lee, Y. Ye and A. J. Ward, *Sep. Purif. Technol.*, 2016, **163**, 109–119.
42 S. Bakhshayesh and H. Dehghani, *J. Iran. Chem. Soc.*, 2014, **11**, 769–780.
43 T. P. Almeida, F. Moro and M. W. Fay, *J. Nanopart. Res.*, 2014, **16**, 1–13.
44 E. Gil, J. Cortés and I. Iturriza, *Appl. Surf. Sci.*, 2018, **427**, 182–191.
45 A. Kumar, N. Yadav, D. S. Rana, P. Kumar, M. Arora and R. P. Pant, *J. Magn. Magn. Mater.*, 2015, **394**, 379–384.
46 N. S. Kanhe, A. Kumar, S. M. Yusuf, A. B. Nawale, S. S. Gaikwad, S. A. Raut, S. V. Bhoraskar, S. Y. Wu, A. K. Das and V. L. Mathe, *J. Alloys Compd.*, 2016, **663**, 30–40.
47 R. Kumar, H. Kumar, R. Raj and S. P. B. Barman, *J. Sol-Gel Sci. Technol.*, 2016, **78**, 566–575.
48 L. C. S. Maria, M. A. S. Costa and J. G. M. Soares, *Polymer*, 2005, **46**, 11288–11293.
49 Q. Wang, J. Yang and Y. Dong, *J. Agric. Food Chem.*, 2015, **63**, 4746–4753.
50 Z. Lu, H. Ming and L. Yang, *RSC Adv.*, 2015, **5**, 47820–47829.
51 Q. Y. Yi, J. H. Ji, B. Shen, C. C. Dong, J. Liu, J. L. Zhang and M. Y. Xing, *J. Environ. Sci. Technol.*, 2019, **53**, 9725.
52 S. Debnath, N. Ballav, H. Nyoni, A. Maity and K. Pillaya, *Appl. Catal., B*, 2015, **163**, 330–342.
53 L. Wang, P. Jin, S. Duan, J. Huang, H. She, Q. Wang and T. An, *Environ. Sci.: Nano*, 2019, **6**, 2652–2661.